Supporting Information

Unraveling microenvironment modification in atomically dispersed bimetallic FeCu catalyst in oxygen reduction reaction

Lingmin Wu[a], Yinghua Wang[a], Chunfeng Shao[b], Fanfei Sun[c,*], Liming Wang[a,*], Baitao Li[a,*]

[a] Guangdong Provincial Key Laboratory of Fuel Cell Technology, School of Chemistry and Chemical Engineering, South China University of Technology, Guangzhou 510640, China

[b] Anhui Province Key Laboratory of Pollutant Sensitive Materials and Environmental Remediation, Department of Materials Science and Engineering, Huaibei Normal University, Huaibei 235000, China

[c] Shanghai Synchrotron Radiation Facility, Shanghai Advanced Research Institute, Chinese Academy of Sciences, Shanghai 201204, P. R. China

*E-mail: btli@scut.edu.cn (Baitao Li), wanglm@scut.edu.cn (Liming Wang), sunfanfei@sinap.ac.cn (Fanfei Sun)

1. Computational methods

Density functional theory (DFT) calculation was performed using the Vienna Ab initio Simulation Package (VASP) with the projector augment wave method. The exchange-correlation functional was simulated with generalized gradient approximation of the Perdew-Burke-Ernzerhof (PBE) functional, and the ion-electronic interactions was described with the Projected Augmented Wave (PAW) potential database. The plane wave-basis cutoff energy was set to 400 eV and the Brillouin zone was sampled using the 2x2x1 Monkhorst-Pack *k*-point mesh. The convergence energy and force were set to 1×10^{-5} eV and 0.02 eV $Å^{-1}$, respectively. The vacuum layer was set to 15 Å to eliminate interactions between periodic structures of surface models.

The oxygen reduction reaction (ORR) for the four-electron pathway in alkaline solution proceeded according to the following equations (Eq. 1-4):

$$O_2(g) + * + H_2O(l) + e^- \rightarrow OOH^* + OH^- \qquad \Delta G_1 \qquad (1)$$

(adsorbed O_2 dissociation and protonation into OOH*)

$$OOH^* + e^- \rightarrow O^* + OH^- \qquad \Delta G_1 \qquad (2)$$

(OOH* decomposition into O*)

$$O^* + e^- + H_2O \rightarrow OH^* + OH^- \qquad \Delta G_3 \qquad (3)$$

(O* protonation into OH*)

$$OH^* + e^- \rightarrow * + OH^- \qquad \Delta G_4 \qquad (4)$$

(OH* detachment into OH^-)

Where * is a free adsorption site on the surface.

The free energy (ΔG) of each elementary step involving proton/electron transfer was carried out with computational hydrogen electrode (CHE) method, and it was computed based on the equation (5):

$$\Delta G = \Delta E_{DFT} + \Delta E_{ZPE} - T\Delta S - eU \qquad (5)$$

Where ΔE_{DFT}, ΔE_{ZPE} and ΔS are electronic energy, zero-point energy, and entropy difference between absorbed intermediate system and catalyst, respectively, T is the temperature (25°C), e is the transferred electron number and U is the applied potential vs RHE.

The adsorption energy (E_{ads}) was calculated according to equation (6):

$$E_{ads} = E_{system} - E_{catalyst} - E_M \qquad (6)$$

Where E_{system}, E_{catalyst} and E_{M} represent the total energy of the adsorbate (M)-containing system, clean catalyst and adsorbate (M), respectively. The lower value of E_{ads}, the stronger interaction between catalyst and M.

2. Experiment

Synthesis of FeCu-NC-*x* catalyst. First, 0.4 g of commercial SiO_2 (Shanghai Aladdin Biochemical Technology Co., Ltd.) was dissolved in 30 mL of EtOH aqueous solution (EtOH:water = 1:1, v:v) and sonicated for 1 h (referred to as solution A). Simultaneously, 0.1g of carboxylation chitosan was dissolved in 30 mL of H_2O and stirred for 1 h (referred to as solution B). Next, the solution A was slowly added into solution B while stirring for another 2 h. After that, 0.25 g of 1,10-phenanthroline, *y* mg of $Fe(NO_3)_3 \cdot 9H_2O$ and 27.6 mg of $Cu(NO_3)_2 \cdot 3H_2O$ were introduced into the mixture, which was stirred continuously at 80°C until the water evaporated completely. Subsequently, the solid was thermally treated under nitrogen atmosphere at 900°C for 2 h with a heating rate of 5°C min^{-1}. It was then leached in 10 wt% of HF for 12 h to remove the SiO_2 template. Finally, the product was obtained after a second pyrolysis at 900°C for 2 h. The amount of $Cu(NO_3)_2·3H_2O$ was kept constant, while the amount of Fe salt was set as 48, 24 and 18 mg respectively. The obtained catalyst was respectively denoted as FeCu-NC-x ($x = 1, 2, 3$), where "x" indicated the molar ratio of Cu to Fe. The Fe-NC and Cu-NC catalyst were also synthesized by the same process, with 48 mg of $Fe(NO_3)_3·9H_2O$ and 27.6 mg of $Cu(NO_3)_2·3H_2O$, respectively.

3. Characterization

The morphological feature was studied using a field emission scanning electron microscope (FE-SEM, SU8220, Hitachi) and a transmission electron microscope (TEM, JEM-2100F, JEOL) equipped with an energy dispersive X-ray spectrometer (EDX, Bruker, XFlash 6T-60). The fine atomic structure was analyzed using an aberration-corrected high-angle annular dark-field scanning transmission electron microscope (HAADF-STEM, Themis Z, FEI). The local coordination site structure and electronic properties of Fe and Cu were investigated via X-ray absorption spectroscopy (XAS) in two spectral regions, the X-ray Absorption Near-Edge Structure (XANES) region and the Extended X-ray Absorption Fine Structure (EXAFS) region. This measurement was conducted at BL20U station of Shanghai Synchrotron Radiation Facilities under fluorescence excitation mode. Furthermore, the crystal structure and phases present in the catalyst were identified by a powder X-ray diffractometer (XRD, D8 Advance, Bruker) in the 2θ range of 5° to 90°. The actual amounts of iron and copper in catalyst were quantified using inductively coupled plasma optical emission spectroscopy (ICP-OES, Optima 8300, PerkinElmer). The surface elemental composition was analyzed by X-ray photoelectron spectroscopy (XPS, ESCALAB 250Xi, Thermo Fisher Scientific) with a monochromatized Al $K\alpha$ source. The specific surface area and pore size distribution were collected by physisorption with nitrogen as adsorbate on an automated surface area and pore size analyzer (ASAP 2460, Micromeritics). The surface area was obtained according to Brunauer-Emmett-Teller (BET) theory and the pore size distribution was based on density functional theory (DFT). Prior to the measurement, the catalyst was pretreated at 100 °C for 6 h under vacuum to remove any species adsorbed on the catalyst surface.

4. Electrochemical measurement

The electrocatalytic activity towards oxygen reduction reaction (ORR) was assessed using a three-electrode system equipped with an electrochemical workstation (IGS-6030, Guangzhou Ingsens Sensor Technology Co., Ltd., China). A glassy carbon working electrode (5 mm diameter) was set in the rotating disk electrode (RDE) measurement. A saturated calomel electrode (SCE) was employed as reference electrode and a carbon rod as the counter electrode. For the synthesized catalyst, the loading on the working electrode was 0.408 mg cm^{-2}, while for the 20 wt% commercial Pt/C catalyst (Shanghai Hesen Electrical Co., Ltd.), it was 0.204 mg cm^{-2}. The electrocatalyst ink was made as a suspension by taking 4 mg of catalyst in 1.0 mL of a 0.25% Nafion solution with ethanol as the solvent. Linear sweep voltammogram (LSV) was performed in O_2-saturated electrolytes at a scan rate of 10 mV s^{-1} at different rotation speeds (625, 900, 1225, 1600, 2025 rpm). The sweep window was spanned from 0.2 to −0.8 V vs. SCE in 0.1 M KOH solution, and from 0.4 to −0.6 V vs. SCE in a neutral 0.05 M phosphate buffered saline (PBS) solution.

The kinetics parameters were determined with Koutechy-Levich equation (Eq. 7-8):

$$\frac{1}{J}=\frac{1}{J_L}+\frac{1}{J_K}=\frac{1}{B\omega^{\frac{1}{2}}}+\frac{1}{J_K} \tag{7}$$

$$B=0.2nFC_0D_0^{\frac{2}{3}}v^{-\frac{1}{6}} \tag{8}$$

Where J, J_L, J_K is the overall measured current density, diffusion-limiting current density and kinetic current density, respectively, ω is the electrode rotation speed (rpm), n is the number of electron transferred in ORR reaction, F is Faraday constant (96485 C mol^{-1}), C_0 is the saturated O_2 concentration in the solution (1.26x10^{-6} mol cm^{-3}), D_0 is the diffusion coefficient of O_2 (2.7 x10^{-5} cm^{2} s^{-1}), v is the kinematic viscosity of electrolyte (0.01 cm^{2} s^{-1}).

The electron transfer number (n) was examined by rotating ring-disk electrode (RRDE) at rotation rate of 1600 rpm with the ring electrode voltage at 1.5 V vs. Reversible hydrogen electrode (RHE). The peroxide yield (HO_2^- %) was obtained from disk (i_d) and ring (i_r) current (Eq. 9-10):

$$n = \frac{4 \mid i_d \mid}{\mid i_d \mid + \frac{i_r}{N}} \tag{9}$$

$$\mathrm{HO_2^-}\% = \frac{2i_r/N}{\mid i_d \mid + \frac{i_r}{N}} \times 100\% \tag{10}$$

Where N is the collection efficiency of Pt ring (N=37%).

The electrochemical surface area (ECSA) was estimated by electrochemical double-layer capacitance (C_{dl}) using cyclic voltammograms (CVs) method with the scan range from 1.0 to 1.1 V vs. RHE. in alkaline electrolyte.

The stability and methanol tolerance were both estimated by current-time (i-t) chronoamperometric method at half-wave potential ($E_{1/2}$). The long-term durability was measured by accelerated durability test (ADT) method with the scan rate of 0.2 V s^{-1} from −0.8 to 0 V vs. SCE in alkaline and 0.4 V to −0.6 V vs. SCE in neutral solution.

5. Zn-Air battery assembly and measurement

A button-type Zn-air battery was assembled using a mixed solution containing 6 M KOH and 2 M $Zn(CH_3COO)_2$ as the electrolyte, 0.2 g of Zn power (99.99%) as the anode, Ni-foam as current collector and carbon paper as gas diffusion layer. The catalyst layer was prepared by dispersing 5 mg of catalyst in a mixed solution containing 40 μL of Nafion, 0.5 mL of ethanol and 0.5 mL of water. The catalyst loading on the Ni-foam and carbon paper was 4 mg cm^{-2} for the resultant catalyst, while 2 mg cm^{-2} in the case of commercial 20 wt% Pt/C. All electrochemical measurements were conducted on an CHI660D electrochemical workstation (Shanghai CH Instrument Co., Ltd.) in room environment.

6. Microbial fuel cell (MFC) construction and measurement

The membraneless single chamber MFC with a volume of 28 mL was used in this study. The MFC was filled with the mixture of effluent from a municipal sewage treatment plant (Guangzhou) and neutral culture medium at a volume ratio of 1:3 as electrolyte. The carbon cloth was colonized with electroactive microbes from anaerobic sewage for at least two months and then transferred to the MFC as the anode, while the catalyst ink loaded on carbon cloth was used as cathode. The carbon cloth was pretreated following our previous work [1].

The catalyst ink was prepared by dispersing each 1 mg of catalyst in a mixture solution of 0.83 μL of water, 6.67 μL of Nafion and 3.33 μL of isopropanol. The loading for prepared catalyst was 4 mg cm^{-2}, while for 20 wt% Pt/C it was set at 2.5 mg cm^{-2}, in alignment with common practices in MFC research [2]. The assembled MFC was placed in the incubator at 37°C and a fixed 1000 Ω of external resistance was used to connect the anode and cathode. The output voltage stability test was recorded by digital multimeter. The polarization curves were measured by varying the external resistance from 33000 to 80 Ω when the voltage reached a platform during the cycles of 2 ~ 4.

The chemical oxygen demand (COD) removal was analyzed using a COD-571 detector (Shanghai Precision and Scientific Instrument Co. China). The COD removal efficiency and Coulombic efficiency (CE) was individually calculated by equation (11) and (12):

$$COD\ removal\ efficiency = \frac{COD_{initial} - COD_{finish}}{COD_{initial}} \tag{11}$$

$$CE = \frac{M\int_0^{t_b} Idt}{FbV_{Anode}\Delta COD} \tag{12}$$

Where $COD_{initial}$ is the sodium acetate-based synthetic wastewater, and the COD_{finish} is the effluent from different MFCs after operation for 2~4 cycles, M is the molecular weight of oxygen ($M = 32$), I is the current corresponding platform period, F is Faraday's constant ($F = 96{,}485$ C mol^{-1}); b is the electrons transferred number ($b = 4$), V_{Anode} is the volume of substrate solution in anode chamber ($V_{Anode} = 28$ mL); ΔCOD is the change of COD value over the corresponding period (t_b).

Figures and Tables

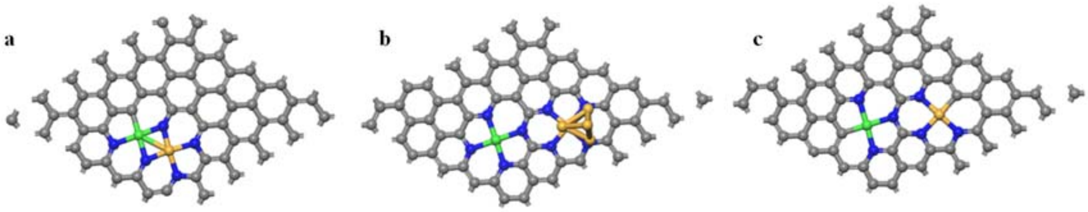

Figure S1. Constructed models for FeCu-dimer (a), Fe_5-CuN_4 (b) and FeCu-isolated (c). Color interpretation: green (Cu atom), yellow (Fe atom), dark blue (N atom), and grey (C atom).

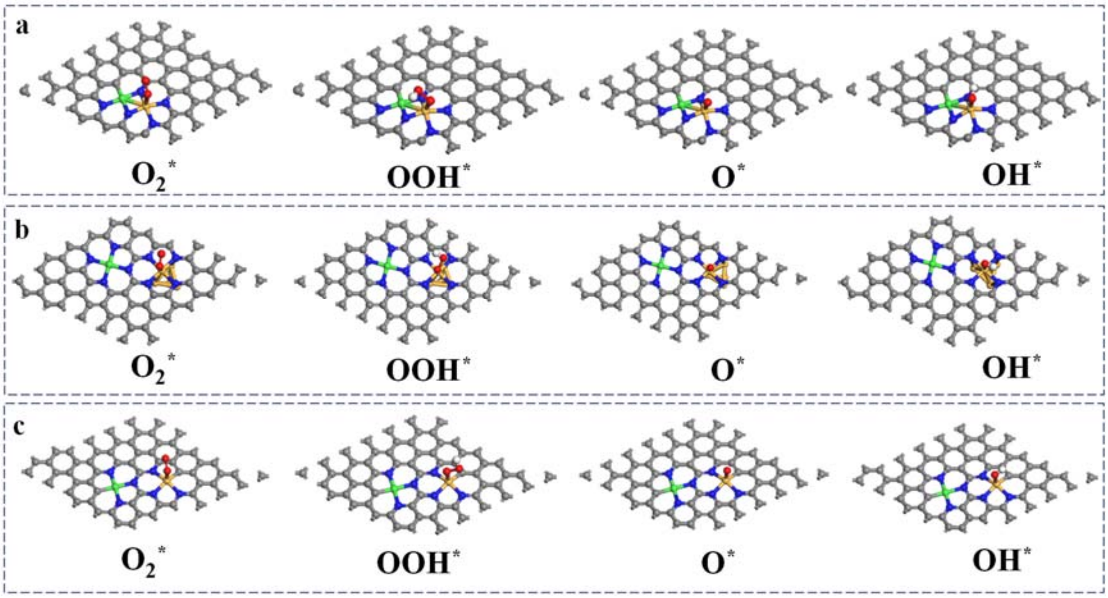

Figure S2. Geometric structures of intermediates adsorbed on FeCu-dimer (a), Fe_5-CuN_4 (b) and FeCu-isolated (c) models. Color interpretation: green (Cu atom), yellow (Fe atom), dark blue (N atom), red (O atom), white (H atom), and grey (C atom)

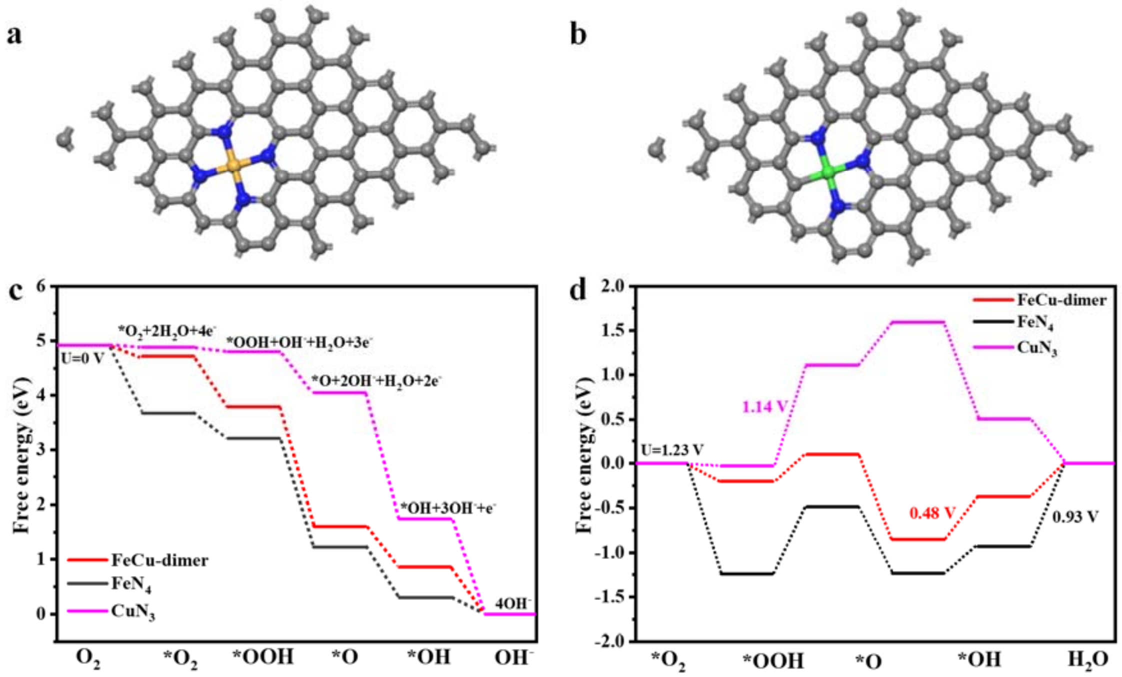

Figure S3. Constructed FeN_4 (a) and CuN_3 (b) models, and their free energy diagram at $U = 0$ V (c) and $U = 1.23$ V (d). Color interpretation: green (Cu atom), yellow (Fe atom), dark blue (N atom), and grey (C atom).

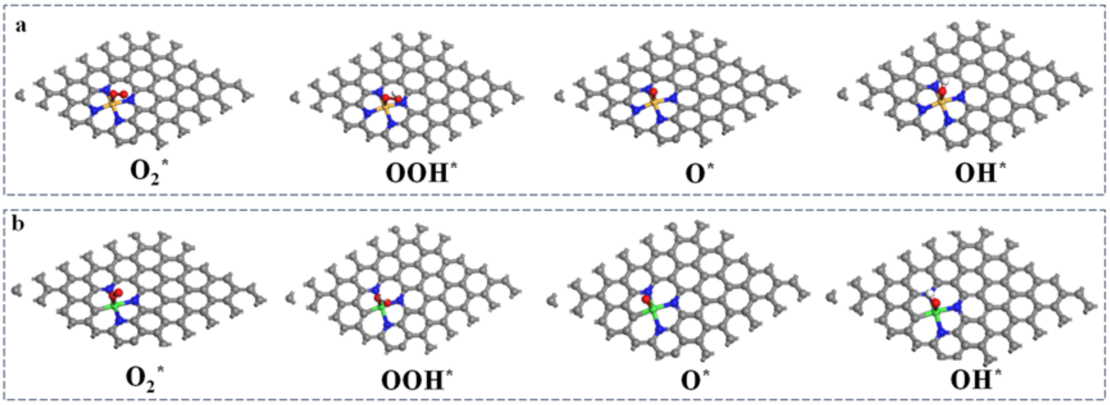

Figure S4. Geometric structures of intermediates adsorbed on FeN_4 (a) and CuN_3 (b) models. Color interpretation: green (Cu atom), yellow (Fe atom), dark blue (N atom), red (O atom), white (H atom), and grey (C atom)

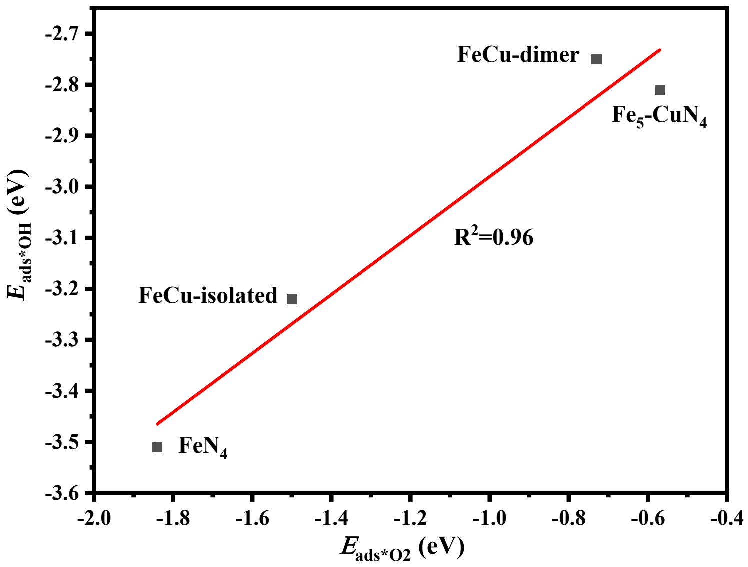

Figure S5. Linear scaling relationship between *OH adsorption energy ($E_{ads,\ *OH}$) versus*O_2 adsorption energy ($E_{ads,*O2}$). Note: CuN_3 was not included in the linear fitting because its adsorption energy for oxygen-containing species was so weak that it did not match with other four Fe-based catalysts.

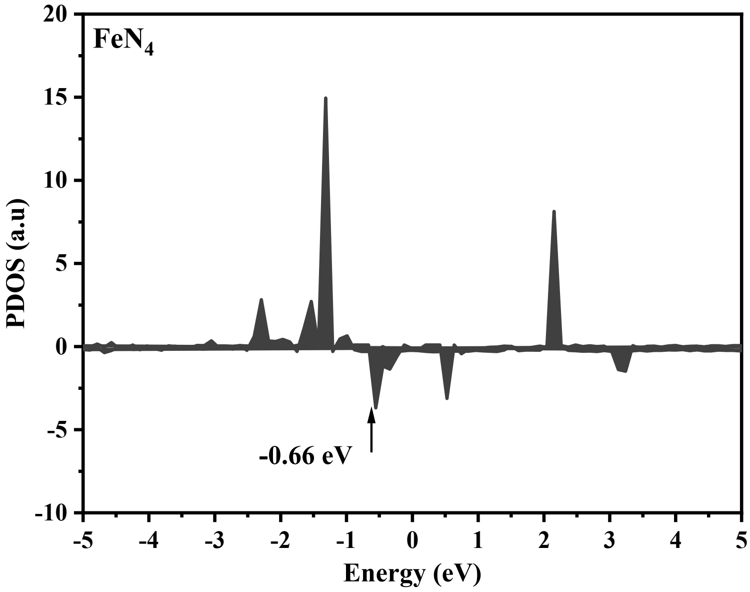

Figure S6. Computed projected density of states of FeN_4 model.

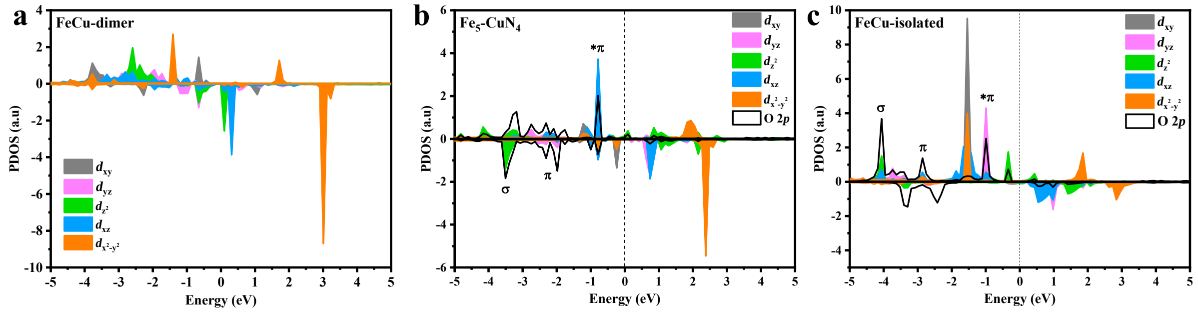

Figure S7. Computed projected density of states of Fe-3*d* of FeCu-dimer before OH adsorbed (a), orbitals interaction between Fe-3*d* and *OH intermediates on Fe$_5$-CuN$_4$ (a) and FeCu-isolated (b).

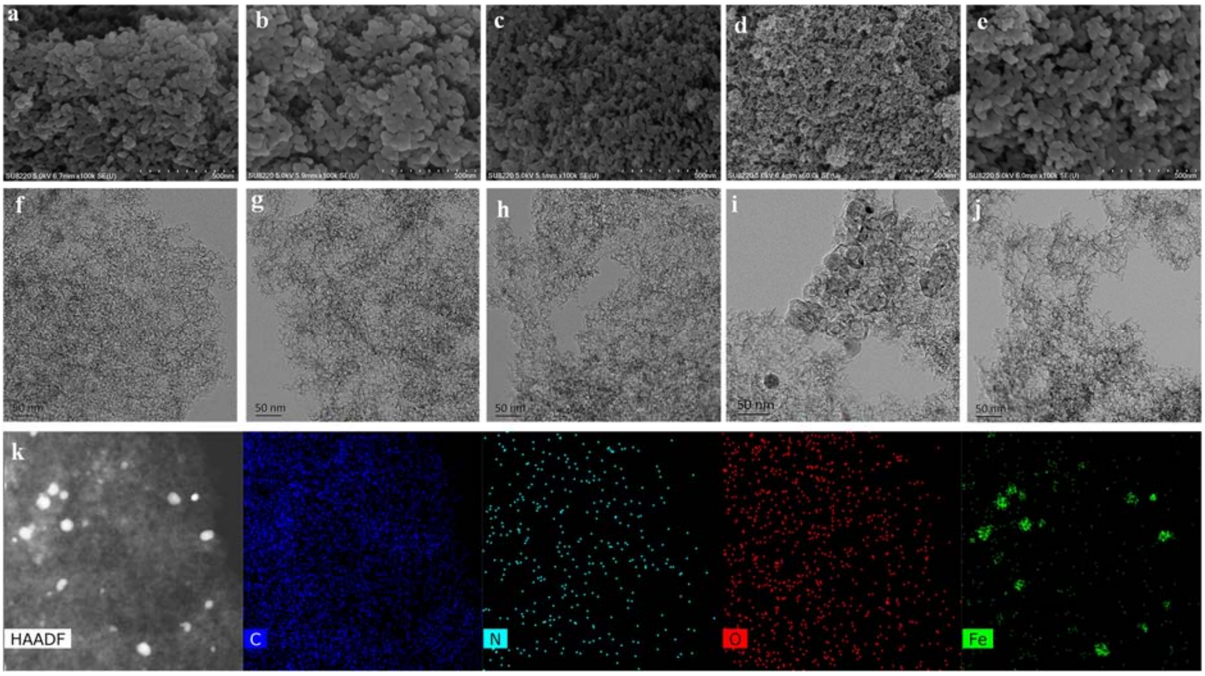

Figure S8. SEM images (a-e) and TEM images (f-j) of FeCu-NC-1 (a, f), FeCu-NC-2 (b, g), FeCu-NC-3 (c, h), Fe-NC (d, i) and Cu-NC (e, j), and HAADF-STEM image and corresponding elements distribution of Fe-NC (k).

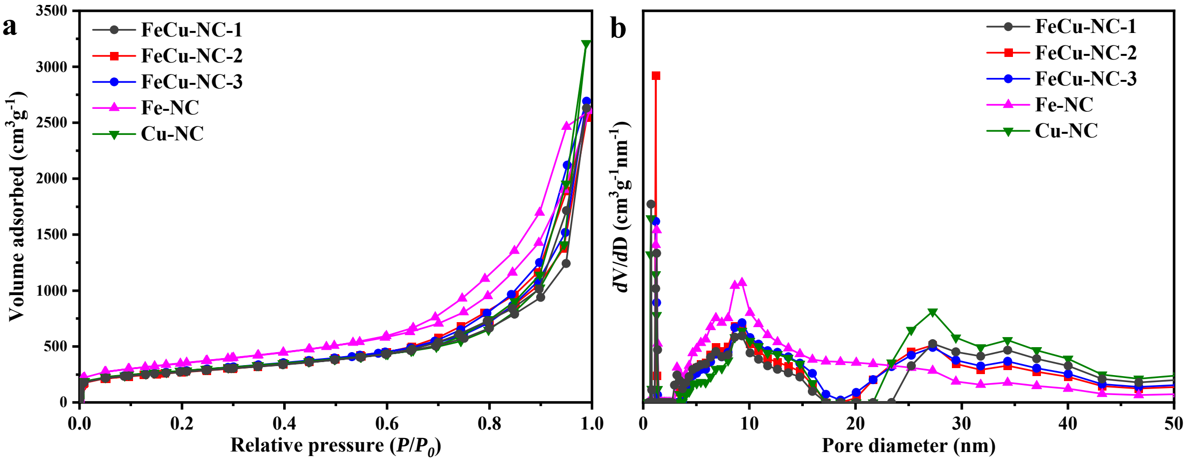

Figure S9. Nitrogen sorption isotherms (a) and the corresponding pore size distribution (b) of FeCu-NC-1, FeCu-NC-2, FeCu-NC-3, Fe-NC and Cu-NC catalysts.

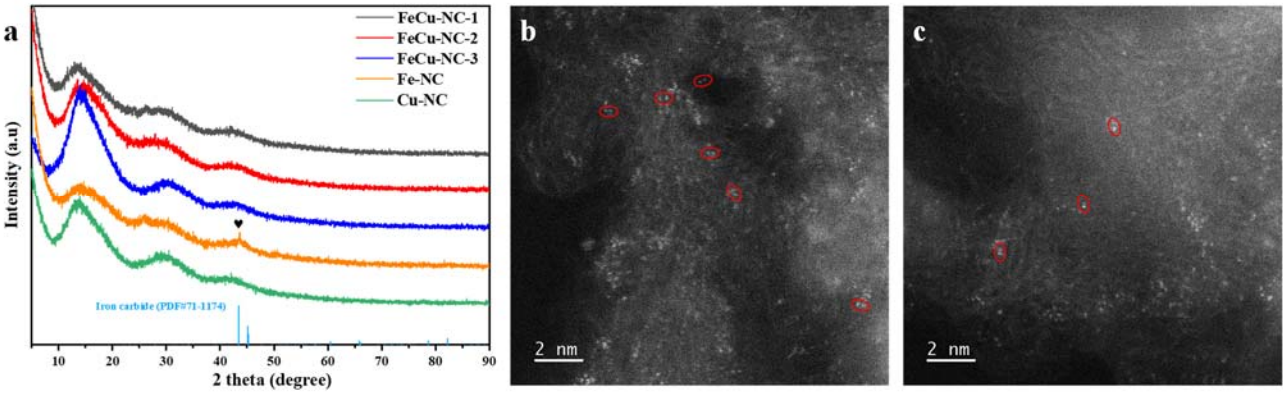

Figure S10. XRD patterns of FeCu-NC-1, FeCu-NC-2, FeCu-NC-3, Fe-NC and Cu-NC catalysts (a) and aberration-corrected HAADF-STEM images of FeCu-NC-2 (b, c).

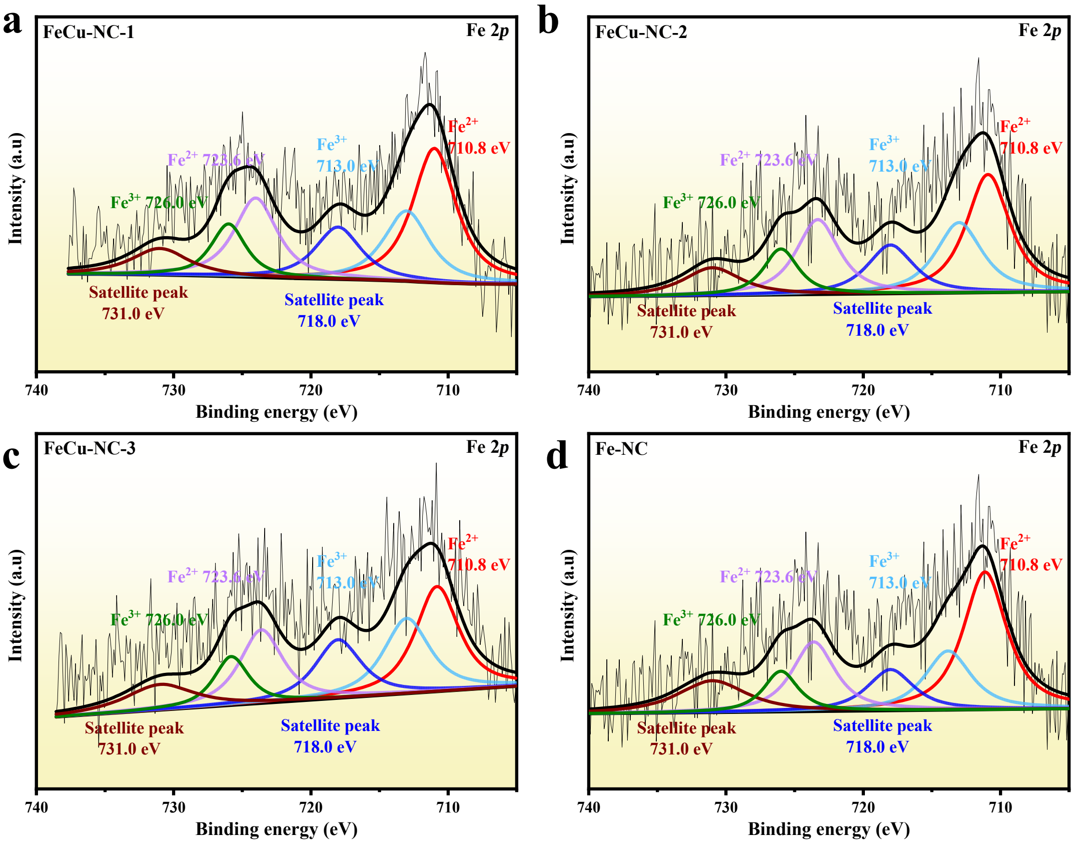

Figure S11. High-resolution scan of Fe 2*p* XPS spectra for FeCu-NC-1 (a), FeCu-NC-2 (b), FeCu-NC-3 (c) and Fe-NC (d) catalysts.

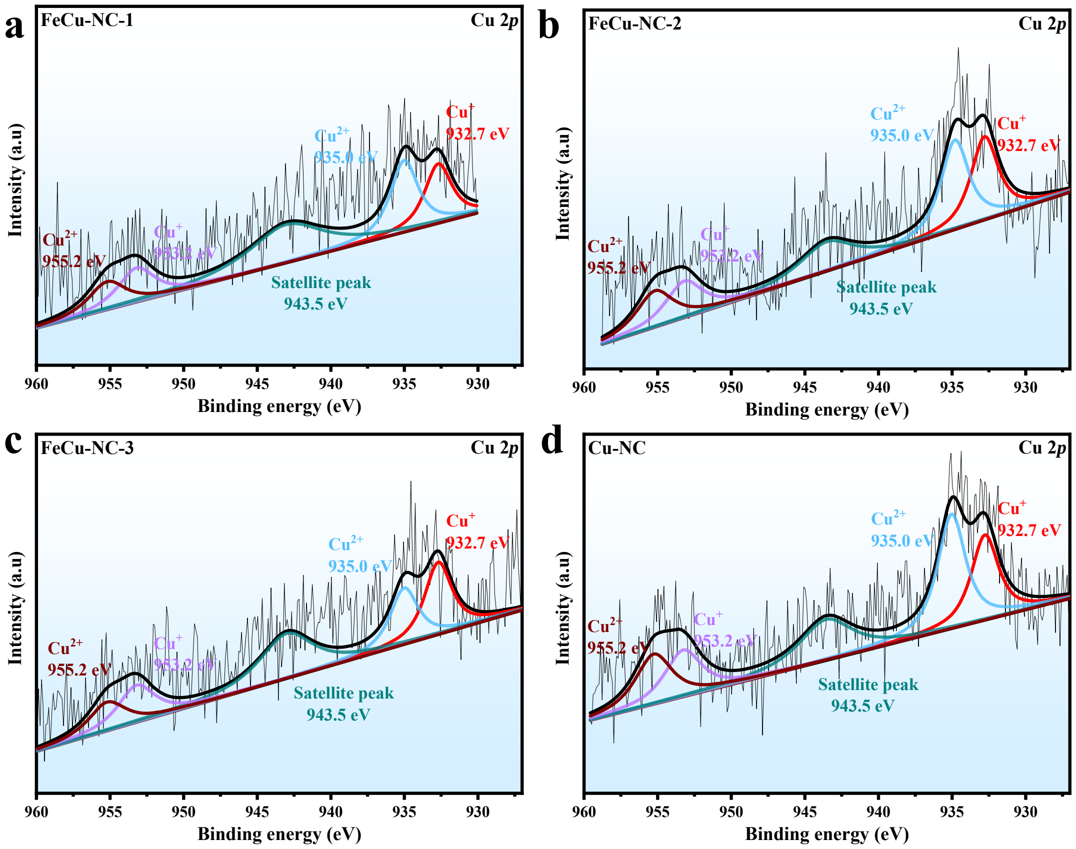

Figure S12. High-resolution scan of Cu 2*p* XPS spectra for FeCu-NC-1 (a), FeCu-NC-2 (b), FeCu-NC-3 (c) and Cu-NC (d) catalysts.

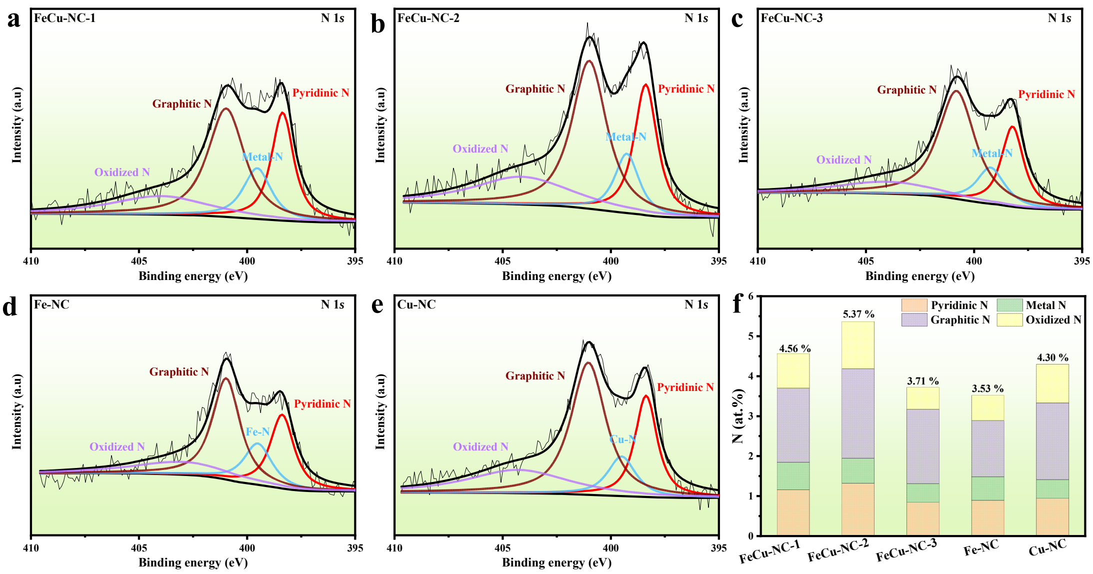

Figure S13. High-resolution scan of N 1*s* XPS spectra for FeCu-NC-*x* catalysts (a, b, c), Fe-NC (d) and Cu-NC (e), and the contents of various nitrogen species detected from XPS analysis (f).

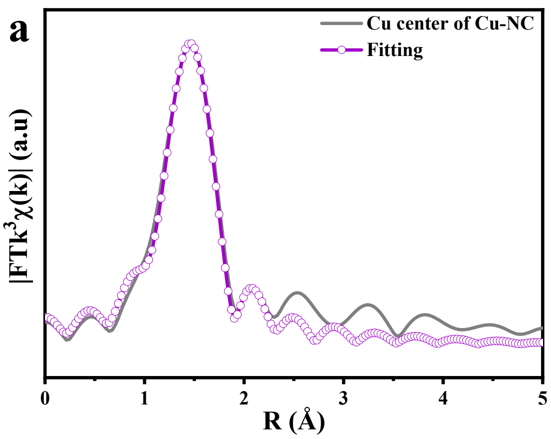

Figure S14. EXAFS fitting spectra (a) and wavelet transforms analysis (b) for Cu-NC.

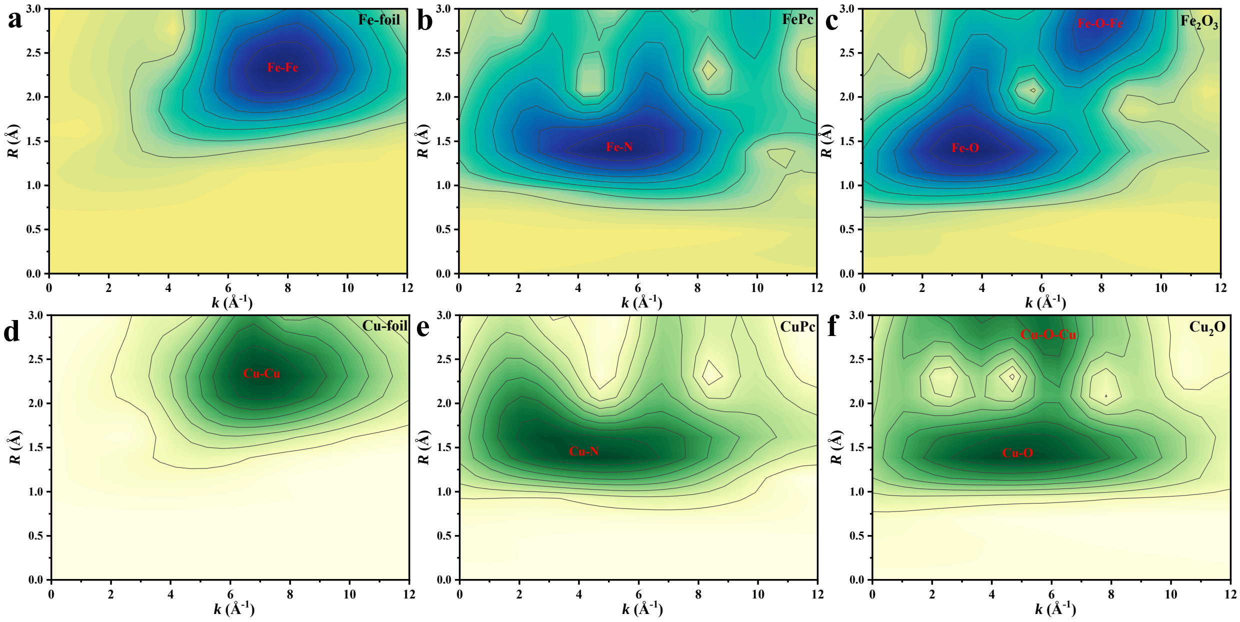

Figure S15. Wavelet transforms analysis for Fe foil (a), FePc (b), Fe_2O_3 (c), Cu foil (d), CuPc (e) and Cu_2O (f) references.

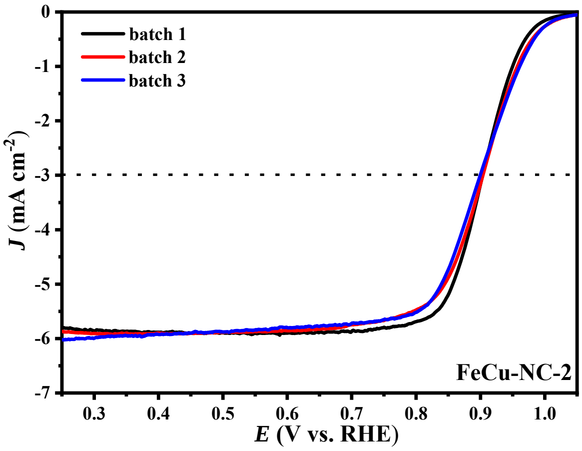

Figure S16. LSV curves at 1600 rpm of different batches of FeCu-NC-2 in 0.1 M KOH.

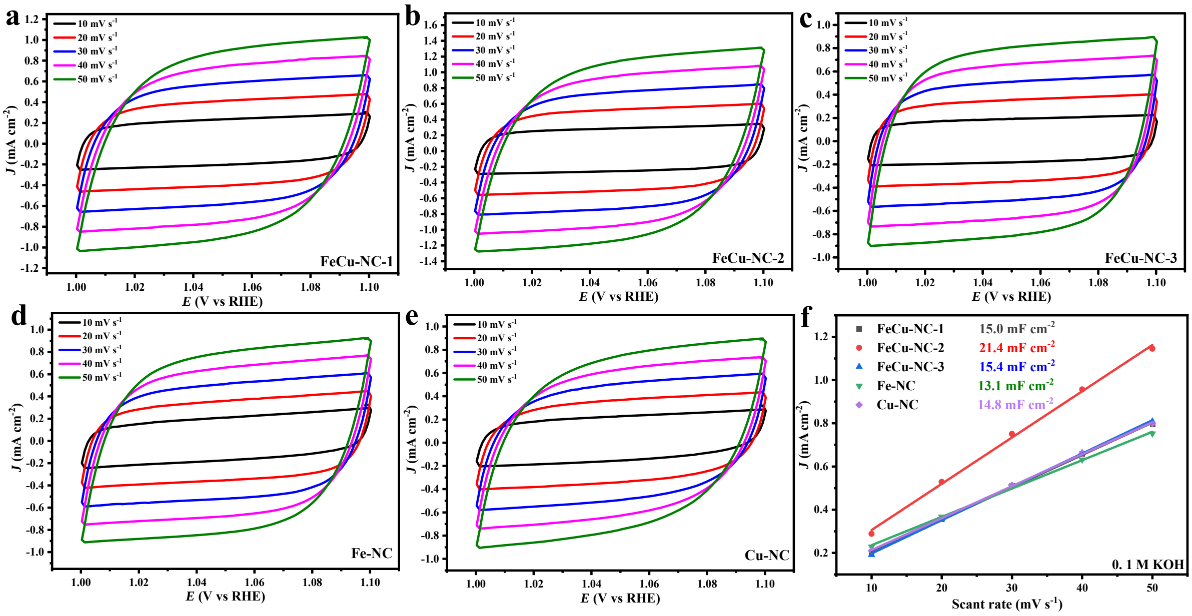

Figure S17. Cyclic voltammograms vs. scan rate in the potential range of 1.00-1.10 V vs. RHE for FeCu-NC-1 (a), FeCu-NC-2 (b), FeCu-NC-1 (c), Fe-NC (d) and Cu-NC (e) in N_2-saturated 0.1 M KOH. Double layer capacitances (C_{dl}) of above catalysts at the potential of ~ 1.05 V vs. RHE. (f).

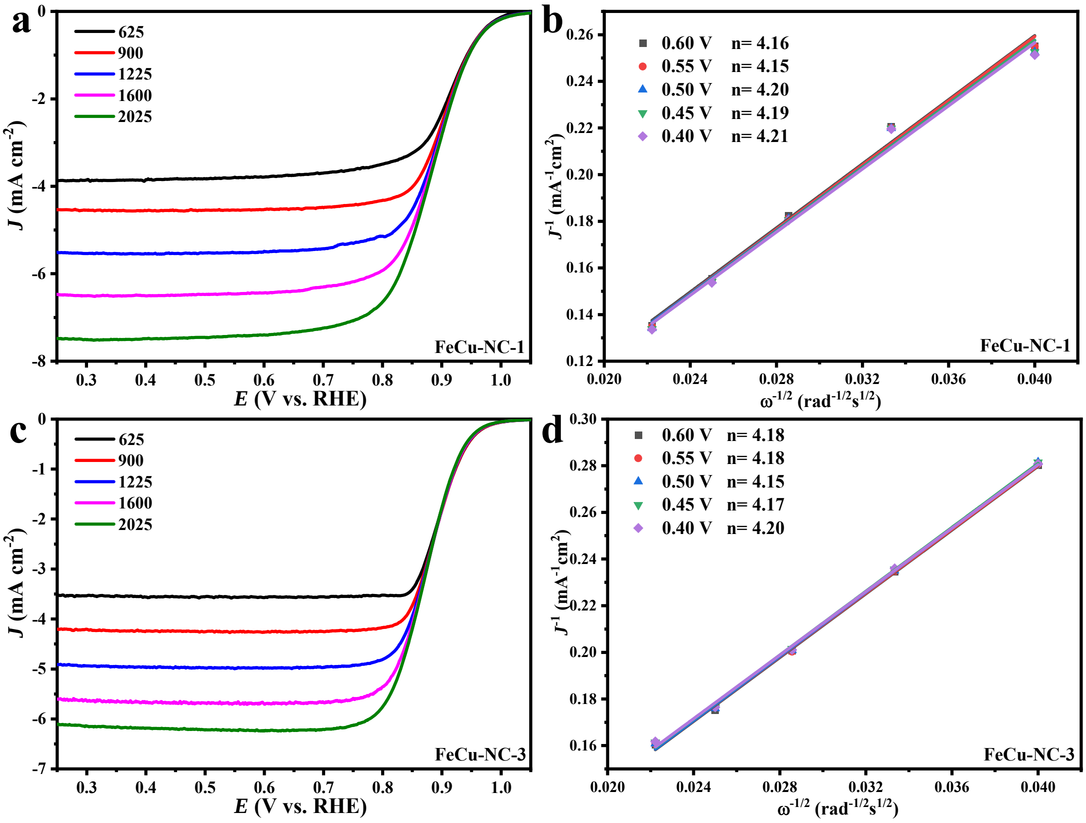

Figure S18. Linear sweep voltammograms at different rotate speed from 625 to 2025 rpm in 0.1 M KOH and the corresponding electron transfer numbers of FeCu-NC-1 (a, b) and FeCu-NC-3 (c, d).

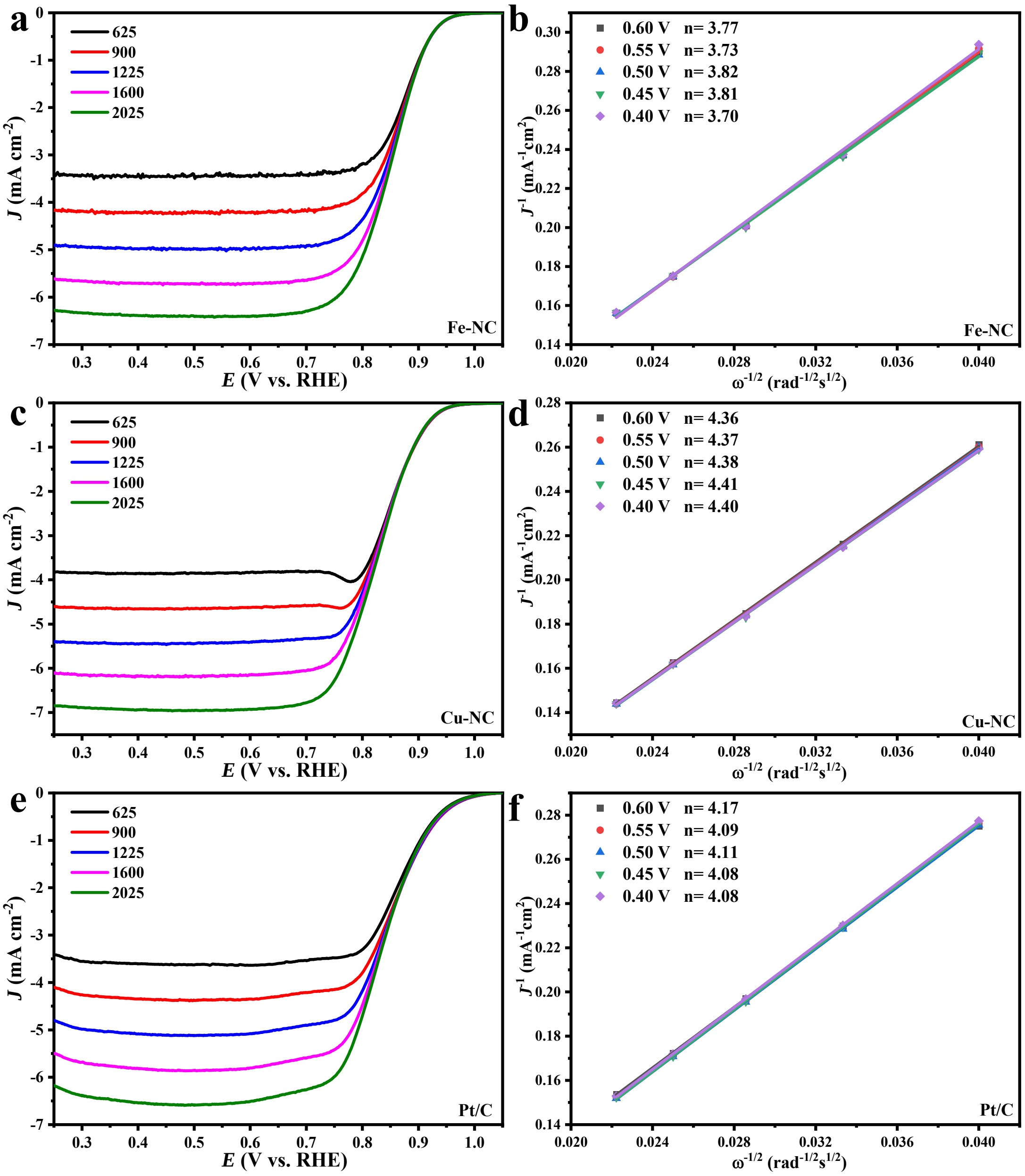

Figure S19. Linear sweep voltammograms at different rotate speed from 625 to 2025 rpm in 0.1 M KOH and the corresponding electron transfer numbers of Fe-NC (a, b), Cu-NC (c, d) and Pt/C (e, f).

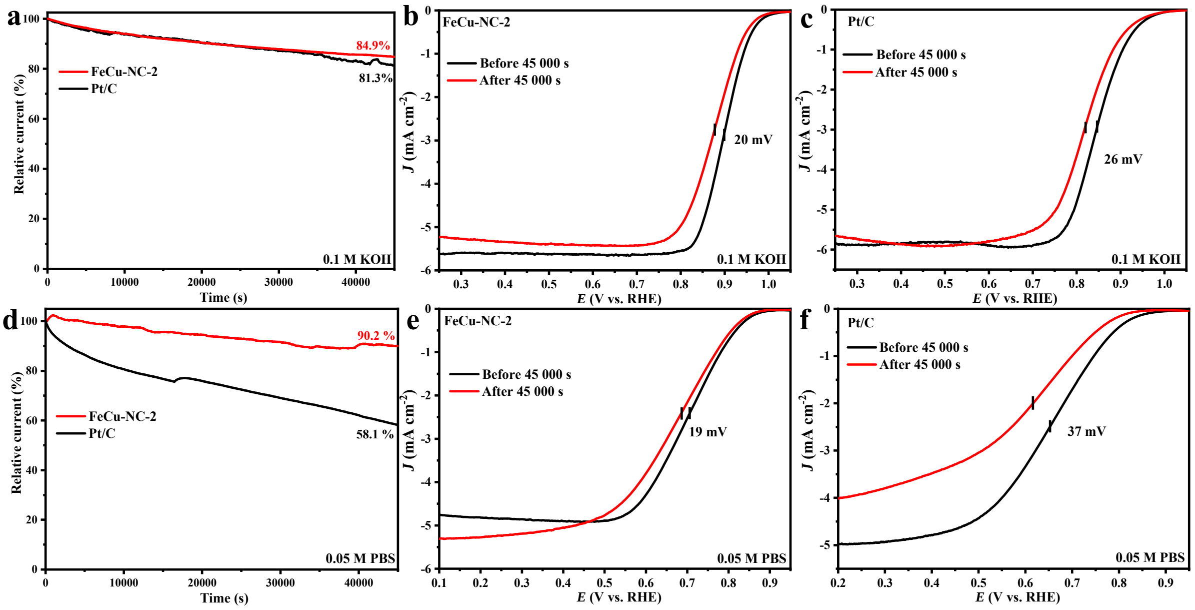

Figure S20. Stability test of FeCu-NC and Pt/C in 0.1 M KOH (a) and 0.05 M PBS (d), and corresponding polarization curves before and after 45000 s (b, c, e, f).

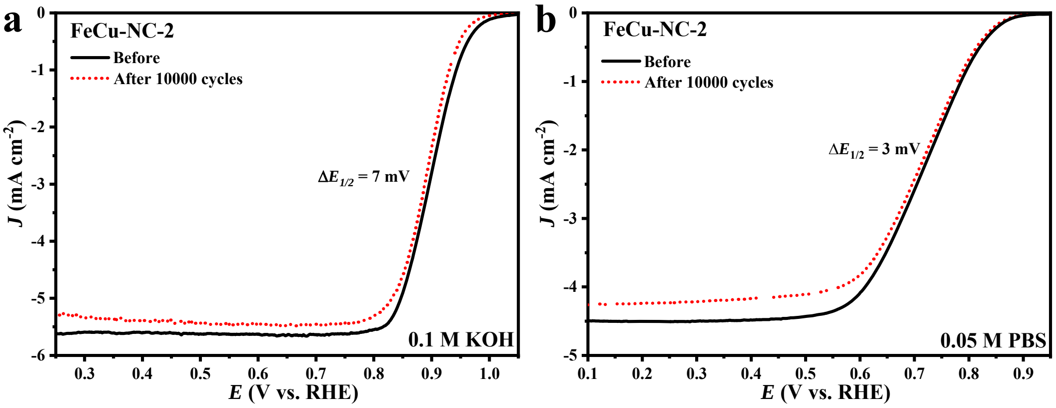

Figure S21. Linear sweep voltammograms of FeCu-NC-2 catalyst before and after 10000 cycles in O_2-saturated 0.1 M KOH (a) and 0.05 M PBS (b).

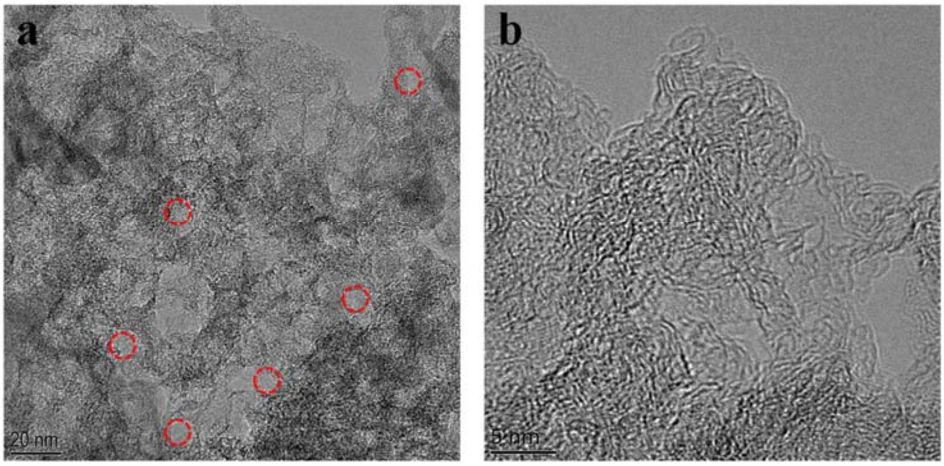

Figure S22. TEM images of FeCu-NC-2 after ADT of 10000 cycles in 0.1 M KOH. Red circles indicated the porous structure.

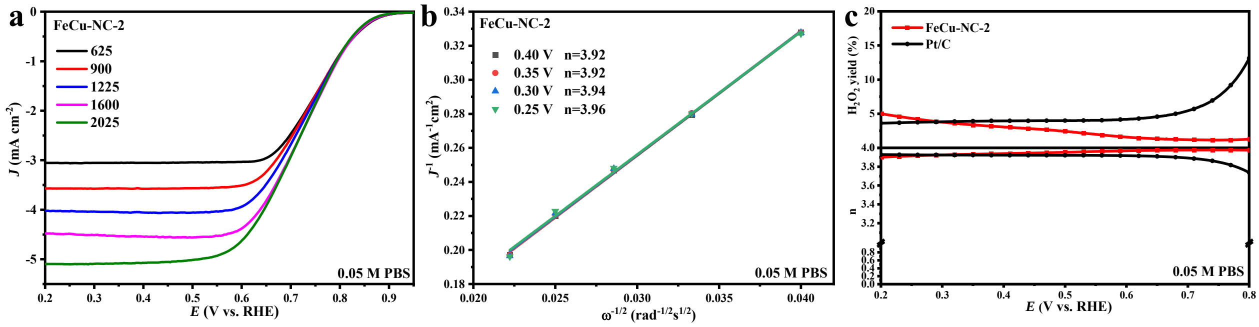

Figure S23. Linear sweep voltammograms of FeCu-NC-2 (a), the corresponding electron transfer numbers from the K-L equation (b), and the RRDE analysis of FeCu-NC-2 and Pt/C reference (c) in 0.05 M PBS solution.

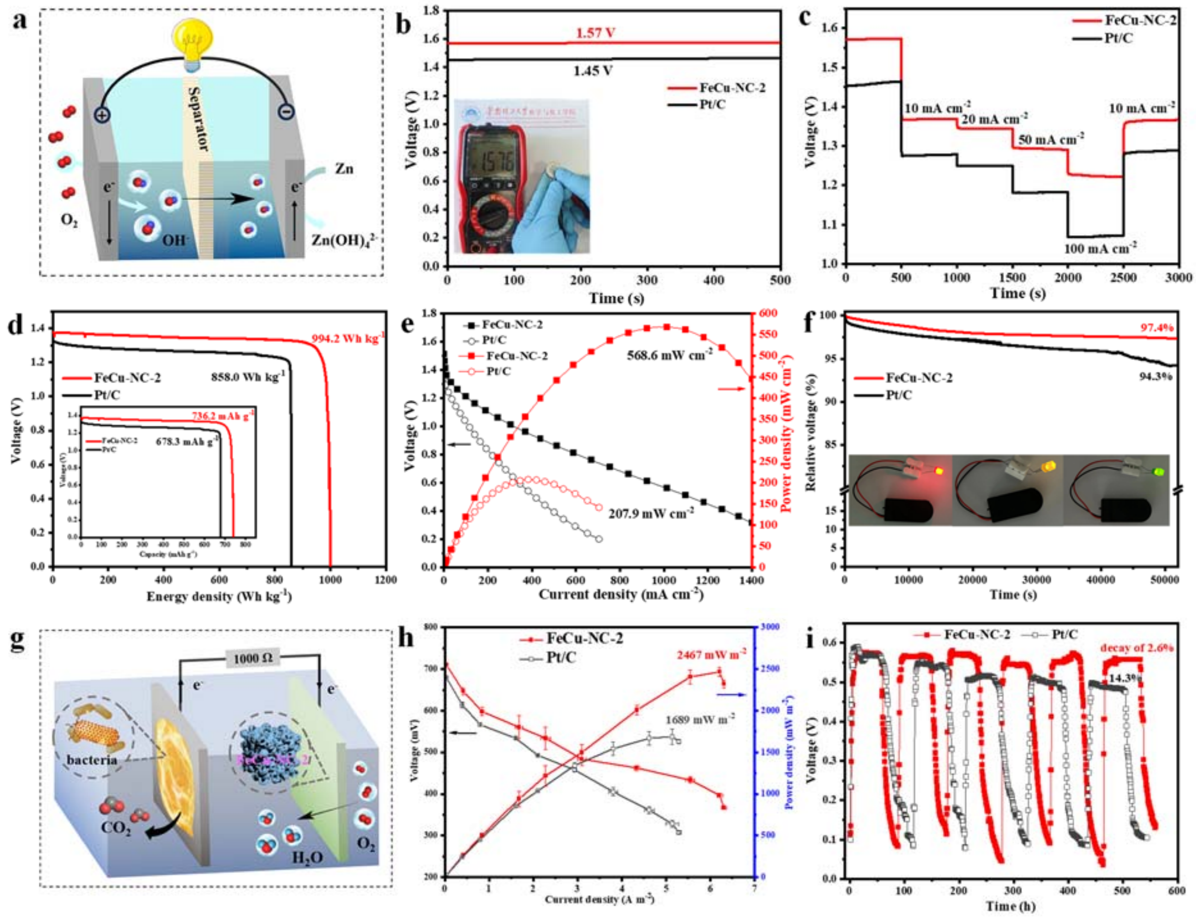

Figure S24. Performance of FeCu-NC-2 and Pt/C based Zn-Air batteries (ZAB) and microbial fuel cells (MFC). Schematic of the assembled ZAB (a), open circuit voltage and the inset showing a FeCu-NC-2-ZAB measured by a multimeter (b), discharge curves at various current density (c), discharge energy density and specific capacity at a discharged current density of 10 mA cm^{-2} (d), polarization and power density plots (e), stability test at 10 mA cm^{-2} (the inset showing the LED lightened by two FeCu-NC-2-ZAB in series) (f) of FeCu-NC-2-ZAB and Pt/C-ZAB. Schematic of the assembled single chamber MFC (g), polarization and power density plots (h), stability test with an external resistance of 1000 Ω (i) of FeCu-NC-2-MFC and Pt/C-MFC.

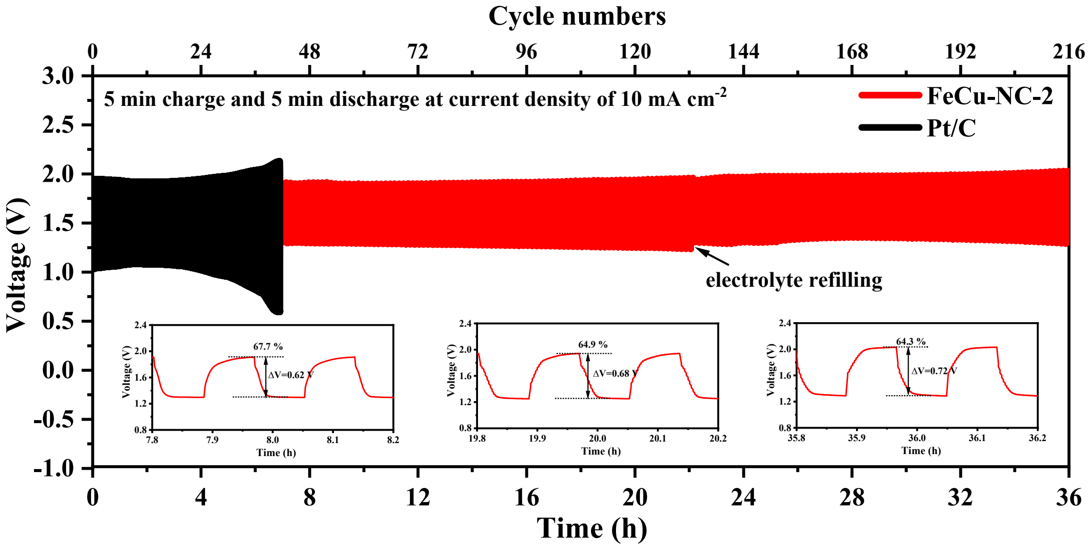

Figure S25. Discharge and charge curves of FeCu-NC-2 and Pt/C at current density of 10 mA cm^{-2}.

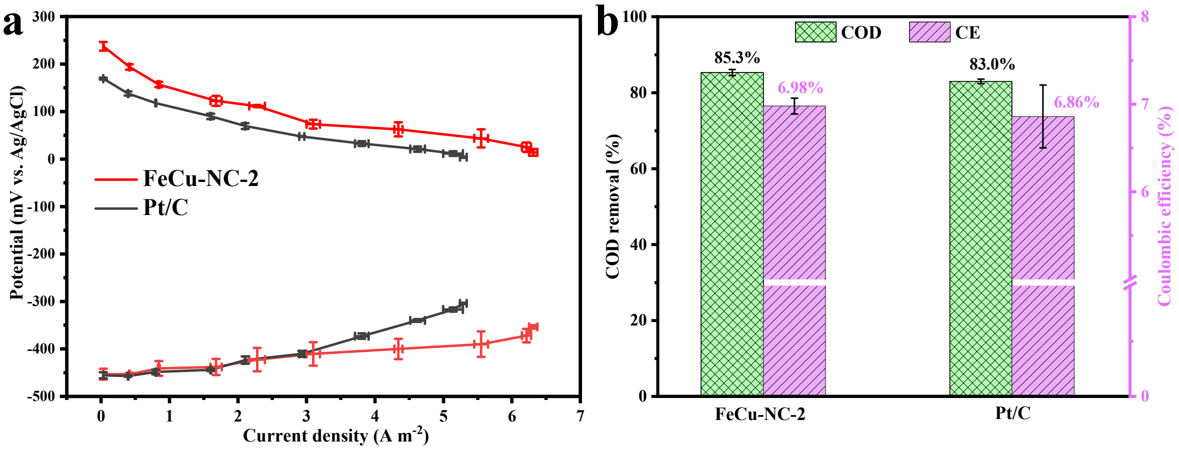

Figure S26. Cathodic and anodic polarization curves (a), and COD removal and CE efficiency (b) of FeCu-NC-2-MFC and Pt/C-MFC.

Table S1. Gibbs free energy change (ΔG), overpotential (η), *d*-band center and adsorption energy for all computed models at $U = 1.23$ V.

Model	ΔG[a] (eV)				η[b] (V)	*d*-band center (eV)	$E_{ads,\ *OH}$ (eV)	$E_{ads,\ *O2}$ (eV)
	ΔG_1	ΔG_2	ΔG_3	ΔG_4				
FeCu-dimer	0.10	-0.95	0.48	0.37	0.48	-1.40	-2.75	-0.73
Fe_5-CuN_4	0.23	0.65	-1.29	0.41	0.65	-1.05	-2.80	-0.57
FeCu-isolated	-0.03	-1.20	0.39	0.84	0.84	-0.73	-3.25	-1.49
Fe-N_4	-0.48	-0.75	0.30	0.93	0.93	-0.66	-3.51	-1.84
Cu-N_3	1.14	0.48	-1.08	-0.51	1.14	/	/	-0.53

[a] Red data indicated the ΔG for the rate-determining step.

[b] Overpotential = $\frac{\mathbf{Max}(\Delta G_1, \Delta G_2, \Delta G_3, \Delta G_4)}{e}$

Table S2. Textural property obtained by physical sorption and metal content analyzed by ICP-OES

Catalyst	S_{surf} ($m^2\ g^{-1}$)	Pore size (nm)	Pore volume ($cm^3\ g^{-1}$)	Fe (wt%)	Cu (wt%)
FeCu-NC-1	948	19.7	4.0	1.85	0.21
FeCu-NC-2	962	17.3	3.9	1.25	0.21
FeCu-NC-3	984	18.6	4.1	0.75	0.23
Fe-NC	1235	10.0	2.9	2.81	/
Cu-NC	975	23.8	4.9	/	0.54

Table S3. Elemental contents detected by XPS analysis

Catalyst	Fe (%)	Fe^{2+}/Fe^{3+}	Cu (%)	Cu^{+}/Cu^{2+}	C (%)	N (%)	O (%)
FeCu-NC-1	0.41	1.83	0.10	0.81	87.37	4.56	7.65
FeCu-NC-2	0.30	1.73	0.12	0.91	87.84	5.37	6.37
FeCu-NC-3	0.22	1.50	0.09	1.24	90.12	3.77	5.80
Fe-NC	0.36	2.18	/	/	89.90	3.53	6.21
Cu-NC	/	/	0.11	0.72	89.44	4.30	6.15

Table S4. Contents (atom%) of nitrogen configurations detected by XPS analysis

Catalyst	Pyridinic N (%)	Metal-N (%)	Graphitic N (%)	Oxidized N (%)	Active N (%)
FeCu-NC-1	1.16	0.68	1.86	0.86	3.70
FeCu-NC-2	1.32	0.63	2.24	1.18	4.19
FeCu-NC-3	0.84	0.47	1.86	0.55	3.17
Fe-NC	0.89	0.59	1.41	0.63	2.89
Cu-NC	0.94	0.47	1.92	0.97	3.33

Table S5. Structural parameters of FeCu-NC-*x* catalysts and Cu-NC extracted from EXAFS fittings

Catalyst	Edge	Path	N[a]	R (Å)[b]	σ^2 (10^{-3}Å^2)[c]	ΔE (eV)[d]	R-factor[e]
FeCu-NC-1	Fe	Fe-N	3.02	1.90	5.61	-14.71	0.018
		Fe-Fe	1.10	2.20	7.18	10.20	
	Cu	Cu-N	3.98	1.97	1.03	-1.40	0.003
FeCu-NC-2	Fe	Fe-N	3.86	1.98	7.00	-3.82	0.015
		Fe-Cu	0.98	1.93	6.42	10.51	
	Cu	$Cu-N_1$	2.20	1.85	0.96	-4.80	0.009
		$Cu-N_2$	0.90	2.23	2.47	-2.51	
		Cu-Fe	1.08	2.31	1.08	3.80	
FeCu-NC-3	Fe	$Fe-N_1$	1.92	1.99	1.91	-1.00	0.004
		$Fe-N_2$	0.93	2.25	1.21	-9.80	
	Cu	$Cu-N_1$	1.80	1.81	1.19	9.02	0.008
		$Cu-N_2$	1.02	2.14	1.82	0.00	
Cu-NC	Cu	Cu-N	4.02	1.95	6.40	-7.35	0.017

[a]N: coordination numbers; [b]R: bond distance; [c]σ^2: Debye-Waller factors; [d]ΔE: the inner potential correction; [e]R-factor: goodness of fit.

Table S6. Comparison of the ORR performance in 0.1 M KOH solution, and ZAB result for FeCu-NC-*x* and similar types of catalysts previously reported.

Catalyst	$E_{1/2}$ (V)	Power density of ZAB (mW cm^{-2})	Reference
Fex/Cu-@CF[a]	0.944	156	3
Fe5-Cu-N-mC[a]	0.92	214.8	4
Cu-N$_x$@Fe$_3$C$_{AC}$[a]	0.89	/	5
Fe-ACSA@NC[a]	0.90	/	6
Fe-AC@Fe-SA-NC[a]	0.912	115	7
FeMn$_{AC}$/Mn-N$_4$C[a]	0.90	207	8
FeCu-NC-1[a]	0.891	/	***This work***
FeCu-SAC[b]	0.926	201.4	9
FeCu SACs/NC[b]	0.89	153	10
CuFe10-900[b]	0.889	200	11
FeCu-NC[b]	0.87	168.1	12
Cu/Zn-NC	0.83	/	13
Ni-N$_4$/GHSs/Fe-N$_4$	0.83	/	14
Fe/Ni-N$_x$/OC	0.938	210	15
FeN$_4$S$_1$/CoN$_4$S$_1$	0.86	152.8	16
Zn/Co-NC	0.938	/	17
FeCu-NC-3[b]	0.877	/	***This work***
FeCu-NC[c]	0.889	91.2	18
FeCu-NC[c]	0.882	/	19
Fe/Cu-N-C[c]	0.879	183	20
Fe, Cu-DAs-NC[c]	0.940	83	21
CoFe-NC[c]	0.94	115	22
Fe-Mn-N-C[c]	0.93	/	23
CuCo-NC[c]	0.89	311.0	24
Cu-Zn-DA/HNC[c]	0.82	170	25
Fe$_2$@PDA-ZIF-900[c]	0.951	/	26
FeNb/c-SNC[c]	0.922	314	27
CoMn-N/S-C[c]	0.883	203	28
Co$_2$-DAs@CHNSs[c]	0.87	69.8	29
FeCu-NC-2[c]	0.904	568.6	***This work***

[a] Clusters and single atoms co-existed in the catalyst;

[b] Isolated dual single atoms co-existed in the catalyst with the atomic distance of > 5 Å;

[c] Dimers existed in the catalyst with the atomic distance of ~ 2.5 Å.

Table S7. Comparison of the ORR performance in neutral solution, and MFC result for FeCu-NC-2 and Fe/Cu doped catalysts previously reported.

Catalyst	$E_{1/2}$ (V)	Power density of MFC (mW m^{-2})	Reference
FeCu@CN	0.547	2796	30
Fe-Cu-NC-50%	/	413	31
Cu@NC	/	1760	32
Cu-NC-800	0.640	663	33
Cu-N/B-C	0.68	760	34
Fe-NC	/	641	35
Fe-N-C	/	1508	36
3D Fe-N-C	0.649	3119	37
FeCu-NC-2	0.720	2467	***This work***

Reference:

1 X. Wang, Z. He, Y. Shi, B. Li, Nitrogen-doped ordered mesoporous carbon as metal-free catalyst for power generation in single chamber microbial fuel cells, *J. Electrochem. Soc.*, 2017, **164**, F620.

2 W. Yang, G. Chata, Y. Zhang, Y. Peng, J.E. Lu, N. Wang, R. Mercado, J. Li, S. Chen, Graphene oxide-supported zinc cobalt oxides as effective cathode catalysts for microbial fuel cell: High catalytic activity and inhibition of biofilm formation, *Nano Energy*, 2019, **57**, 811-819.

3 S. Wu, S. Jiang, S. Liu, X. Tan, N. Chen, J. Luo, S. Mushrif, K. Cadien, Z. Li, Single Cu–N_4 sites enable atomic Fe clusters with high-performance oxygen reduction reactions, *Energy Environ. Sci.*, 2023, **16**, 3576-3586.

4 C. Qi, H. Yang, Z. Sun, H. Wang, N. Xu, G. Zhu, L. Wang, W. Jiang, X. Yu, X. Li, Q. Xiao, P. Qiu, W. Luo, Modulating electronic structures of iron clusters through orbital rehybridization by adjacent single copper sites for efficient oxygen reduction, *Angew. Chem. Int. Ed. Engl.*, 2023, **62**, e202308344.

5 H. Wang, L. Wei, B. Duan, J. Liu, J. Shen, Prussian blue analogue $Cu_3[Fe(CN)_6]_2$ derived N-doped Cu/Fe_3C clusters as an excellent non-noble metal ORR catalyst for microbial fuel cells, *J. Electroanal. Chem.*, 2020, **877**, 114556.

6 H. Huang, D. Yu, F. Hu, S.C. Huang, J. Song, H.Y. Chen, L.L. Li, S. Peng, Clusters induced electron redistribution to tune oxygen reduction activity of transition metal single-atom for metal–air batteries, *Angew. Chem. Int. Ed.*, 2022, **61**, e202116068.

7 X. Ao, W. Zhang, Z. Li, J.-G. Li, L. Soule, X. Huang, W.-H. Chiang, H.M. Chen, C. Wang, M. Liu, Markedly enhanced oxygen reduction activity of single-atom Fe catalysts via integration with Fe nanoclusters, *ACS nano*, 2019, **13**, 11853-11862.

8 H. Liu, L. Jiang, J. Khan, X. Wang, J. Xiao, H. Zhang, H. Xie, L. Li, S. Wang, L. Han, Decorating Single-Atomic Mn Sites with FeMn Clusters to Boost Oxygen Reduction Reaction, *Angew. Chem.*, 2023, **135**, e202214988.

9 H. Yang, H. Huang, Q. Wang, L. Shang, T. Zhang, S. Wang, Fe, Cu dual-metal single atom catalyst on commercial carbon black for efficient oxygen reduction reaction, *J. Mater. Chem. A*, 2023, **11**, 6191-6197.

10 H. Liu, L. Jiang, Y. Wang, X. Wang, J. Khan, Y. Zhu, J. Xiao, L. Li, L. Han, Boosting oxygen reduction with coexistence of single-atomic Fe and Cu sites decorated nitrogen-doped porous carbon, *Chem. Eng. J.*, 2023, **452**, 138938.

11 H. Yang, T. Zhang, X. Chi, X. Yu, J. Chen, J. Chen, C. Li, S. Tan, Q. He, X. Wang, L. Wang, Promoting oxygen reduction via coordination environment modulation through secondary metal-atom incorporation, *J.*

Mater. Chem. A, 2022, **10**, 19626-19634.

12 X. Zhou, K. Song, Y. Feng, C. Jiang, Z. Chen, Z. Wang, N. Yue, X. Ge, W. Zhang, W. Zheng, Individually-atomic governing d—π* orbital interactions via Cu-promoted optimization of Fe-d band centers for high-efficiency zinc-air battery, *Nano Res.*, 2023, **16**, 4634-4642.

13 M. Tong, F. Sun, Y. Xie, Y. Wang, Y. Yang, C. Tian, L. Wang, H. Fu, Operando cooperated catalytic mechanism of atomically dispersed $Cu-N_4$ and $Zn-N_4$ for promoting oxygen reduction reaction, *Angew. Chem. Int. Ed.*, 2021, **60**, 14005-14012.

14 J. Chen, H. Li, C. Fan, Q. Meng, Y. Tang, X. Qiu, G. Fu, T. Ma, Dual single-atomic $Ni-N_4$ and $Fe-N_4$ sites constructing Janus hollow graphene for selective oxygen electrocatalysis, *Adv. Mater.*, 2020, **32**, 2003134.

15 Z. Zhu, H. Yin, Y. Wang, C.H. Chuang, L. Xing, M. Dong, Y.R. Lu, G. Casillas-Garcia, Y. Zheng, S. Chen, Coexisting single-atomic Fe and Ni sites on hierarchically ordered porous carbon as a highly efficient ORR electrocatalyst, *Adv. Mater.*, 2020, **32**, 2004670.

16 Y. Wu, C. Ye, L. Yu, Y. Liu, J. Huang, J. Bi, L. Xue, J. Sun, J. Yang, W. Zhang, Soft template-directed interlayer confinement synthesis of a Fe-Co dual single-atom catalyst for Zn-air batteries, *Energy Storage Mater.*, 2022, **45**, 805-813.

17 W. Xu, R. Zeng, M. Rebarchik, A. Posada-Borbón, H. Li, C.J. Pollock, M. Mavrikakis, H.D. Abruña, Atomically dispersed Zn/Co–N–C as ORR electrocatalysts for alkaline fuel cells, *Journal of the American Chemical Society*, 2024, **146**, 2593-2603.

18 M. Xu, L. Zhang, X. Liang, H. Xiao, H. Zhuang, F. Zhang, T. Zhang, P. Han, W. Dai, F. Gao, J. Zhang, L. Zheng, Q. Gao, Dual-atom $Fe(II,III)N_2(\mu_2\text{-}N)_2Cu(I,II)N$ moieties anchored on porous N-doped carbon driving high-efficiency oxygen reduction reaction, *Appl. Catal. B-Environ. Energy*, 2024, **349**, 123866.

19 Z. Xiao, P. Sun, Z. Qiao, K. Qiao, H. Xu, S. Wang, D. Cao, Atomically dispersed Fe-Cu dual-site catalysts synergistically boosting oxygen reduction for hydrogen fuel cells, *Chem. Eng. J.*, 2022, **446**, 137112.

20 M. Bu, Y. Liu, S. Liao, W. Liu, Z. Yang, J. Jiang, X. Gao, Y. Yang, H. Liu, In-site grown carbon nanotubes connecting Fe/Cu-NC polyhedrons as robust electrocatalysts for Zn-air batteries, *Carbon*, 2023, **214**, 118365.

21 F. Kong, M. Wang, Y. Huang, G. Meng, M. Chen, H. Tian, Y. Chen, C. Chen, Z. Chang, X. Cui, Cu-N-bridged Fe-3d electron state regulations for boosted oxygen reduction in flexible battery and PEMFC, *Energy Storage Mater.*, 2023, **54**, 533-542.

22 K. Wang, J. Liu, Z. Tang, L. Li, Z. Wang, M. Zubair, F. Ciucci, L. Thomsen, J. Wright, N.M. Bedford, Establishing structure/property relationships in atomically dispersed Co–Fe dual site M–N x catalysts on microporous carbon for the oxygen reduction reaction, *J. Mater. Chem. A*, 2021, **9**, 13044-13055.

23 S. Huang, Z. Qiao, P. Sun, K. Qiao, K. Pei, L. Yang, H. Xu, S. Wang, Y. Huang, Y. Yan, The strain induced synergistic catalysis of FeN_4 and MnN_3 dual-site catalysts for oxygen reduction in proton-/anion-exchange membrane fuel cells, *Appl. Catal. B-Environ.*, 2022, **317**, 121770.

24 Z. Ma, R. Bai, W. Yu, G. Li, C. Meng, Copper-cobalt diatomic bifunctional oxygen electrocatalysts based on three-dimensional porous nitrogen-doped carbon frameworks for high-performance zinc-air batteries, *J. Colloid Interf. Sci.*, 2025, **683**, 1150-1161.

25 K. Wu, S. Li, C. Hu, G. Wen, X. Zeng, M. Wang, J. Wang, M. Chu, H. Shang, M. Ye, Nitrogen-bridged Cu-Zn dual-atom cooperative interface sites for efficient oxygen reduction reaction in Zn-air battery, *Appl. Catal. B-Environ. Energy*, 2024, **357**, 124288.

26 K. Leng, J. Zhang, Y. Wang, D. Li, L. Bai, J. Shi, X. Li, L. Zheng, J. Bai, Y. Qu, Interfacial cladding engineering suppresses atomic thermal migration to fabricate well-defined dual-atom electrocatalysts, *Adv. Funct. Mater.*, 2022, **32**, 2205637.

27 R. Sui, B. Liu, C. Chen, X. Tan, C. He, D. Xin, B. Chen, Z. Xu, J. Li, W. Chen, Constructing Asymmetric Fe–

Nb Diatomic Sites to Enhance ORR Activity and Durability, *Journal of the American Chemical Society*, 2024, **146**, 26442-26453.

28 C. Sun, Y. Liu, Z. Lv, R. Liu, C. Wang, L. Li, J. Wang, Y. Zhang, W. Yang, B. Wang, Coordination-environment regulation of atomic Co-Mn dual-sites for efficient oxygen reduction reaction, *Nano Res.*, 2024, 1-8.

29 T. Lu, Q. Zhou, J. Li, T. Li, J. Gong, S. Zhang, H. Pang, S. Xi, L. Xu, G. Luo, Self-Adjustment of Intrinsic Reaction Intermediate on Atomically Dispersed Co2–N6 Binuclear Sites Achieving Boosted Electrocatalytic Oxygen Reduction Performance, *Adv. Funct. Mater.*, 2024, **34**, 2405564.

30 H. Li, H. Shi, Y. Dai, H. You, S.R.B. Arulmani, H. Zhang, C. Feng, L. Huang, T. Zeng, J. Yan, A co-doped oxygen reduction catalyst with FeCu promotes the stability of microbial fuel cells, *J. Colloid Interf. Sci.*, 2022, **628**, 652-662.

31 L. Ren, J. Lu, H. Liu, Activated carbon supported Fe–Cu–NC as an efficient cathode catalyst for a microbial fuel cell, *New J. Chem.*, 2022, **46**, 21579-21590.

32 M. Zhong, C. Ren, D. Fang, C. Lv, K. Li, Cu, N-codoped carbon rod as an efficient electrocatalyst used in air-cathode for high performance of microbial fuel cells, *J. Electroanal. Chem.*, 2020, **878**, 114570.

33 C. Su, W. Wang, B. Jiang, M. Zhang, Y. Wang, H. Wang, H. Song, Fabrication of multi-pore structure Cu, N-codoped porous carbon-based catalyst and its oxygen reduction reaction catalytic performance for microbial fuel cell, *Electroanalysis*, 2023, **35**, e202200266.

34 Q.-R. Pan, B.-L. Lai, L.-J. Huang, Y.-N. Feng, N. Li, Z.-Q. Liu, Regulating the electronic structure of Cu–Nx active sites for efficient and durable oxygen reduction catalysis to improve microbial fuel cell performance, *ACS Appl. Mater. Interfaces*, 2022, **15**, 1234-1246.

35 H. Li, X. Zhang, Y. Qin, Y. Liu, J. Wang, L. Peng, C. Li, Crafting controllable Fe-based hierarchically organic-frameworks from bacterial cellulose nanofibers for efficient electrocatalysts in microbial fuel cells, *J. Power Sources*, 2021, **512**, 230522.

36 D. Wang, H. Liu, Z. Cao, T. Cai, P. Han, J. Song, L. Kong, C. Liu, Ordered porous nitrogen-doped carbon with atomically dispersed FeN_4 for efficient oxygen reduction reaction in microbial fuel cell, *Sci. Total Environ.*, 2022, **838**, 156186.

37 H. Tang, Y. Zeng, Y. Zeng, R. Wang, S. Cai, C. Liao, H. Cai, X. Lu, P. Tsiakaras, Iron-embedded nitrogen doped carbon frameworks as robust catalyst for oxygen reduction reaction in microbial fuel cells, *Appl. Catal. B-Environ.*, 2017, **202**, 550-556.